

Transboundary Storm Risk and Impact Assessment in Alpine Regions



# REPORT ON STORM HAZARD AND CLIMATE CHANGE

REVISION n.: 1		DATE: 30/04/2022	
DISSEMINATION LEVEL: Consortium		WP: 2	TASK(s): 2.1, 2.3
AUTHORS:	Sebastian Lehner, Katharina Enigl, Klaus Haslinger		

Project duration: January 1<sup>st</sup> 2021 – December 31<sup>st</sup> 2022 (24 Months)

## TABLE OF CONTENTS

1. INTRODUCTION .....	3
2. DATA .....	5
GCM data .....	5
Observational Data - SPARTACUS .....	6
Reanalysis Data – JRA-55 .....	6
3. METHODOLOGY .....	7
Quality Control of GCMs.....	7
Downscaling.....	8
Derivation of Hazard Development Corridors .....	10
Climate change assessment.....	<b>Error! Bookmark not defined.</b>
4. RESULTS.....	11
Quality Control of GCMs.....	11
Downscaling.....	12
Derivation of Hazard Development Corridors and Climate Change Assessment.....	15
5. REFERENCES.....	22

## 1. INTRODUCTION

The focus of this report is threefold. The first focal point comprises the selection of ensembles of GCM runs driven with different climate scenarios based on a strict quality control. Secondly, the identified ensembles of large-scale scenarios simulated with global climate models at the world's largest data centers are downscaled to the spatial scale needed for risk assessment in the target regions South Tyrol and East Tyrol/Carinthia using the analog method. This step ensures the physical consistency of the ensembles of regional scale climate change projections associated with the considered SSPs. The third focus lies on the derivation of so-called Hazard Development Corridors (HDCs). These corridors indicate potential trends in future vulnerability (threat levels) to which sustainable conservation strategies and adaptation measures should be aligned. Future changes in hazard potentials generally turn out differently for different damaging processes, categories, regions, as well as pathways of humanity. The two time horizons considered are near future (2036-2065), as well as far future (2071-2100). Based on the Hazard Development Corridors, the potential impact per category can be estimated in terms of frequency changes of potentially damaging weather events.

HDCs are calculated based on the Hazard Trigger Patterns found for two damage event categories (floods and mass movements) in the two target regions South Tyrol (hereafter referred to as “ST”) and East Tyrol – Carinthia (hereafter called “ET\_C”) for the four seasons DJF, MAM, JJA and SON. We derive HTPs via blending damage data with exact temporal and spatial information with meteorological datasets. For the detailed methodology, refer to Deliverable 2.1.

Figures 1 and 2 provide examples for derived hazard trigger patterns during summer months in the target region East Tyrol – Carinthia for the hazard category “flood” and “mass\_movement, respectively.

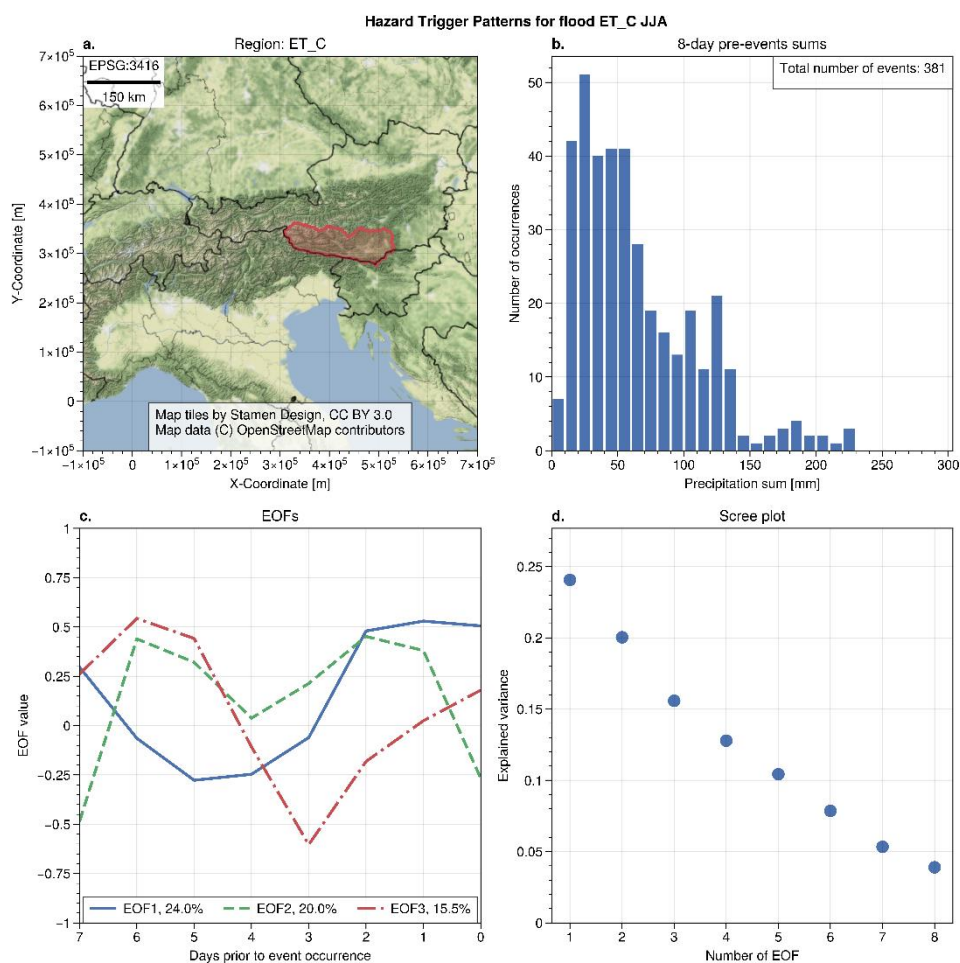


Fig. 1: Hazard Trigger Patterns for the hazard category „Floods“ in the target region „East Tyrol – Carinthia“. a) depicts the region of interest, b) a histogram, showing the precipitation sum of the eight days before an event, c) the three leading EOFs, depicting the preceding weather sequence, and d) the scree plot examining the explained variances of the EOFs.

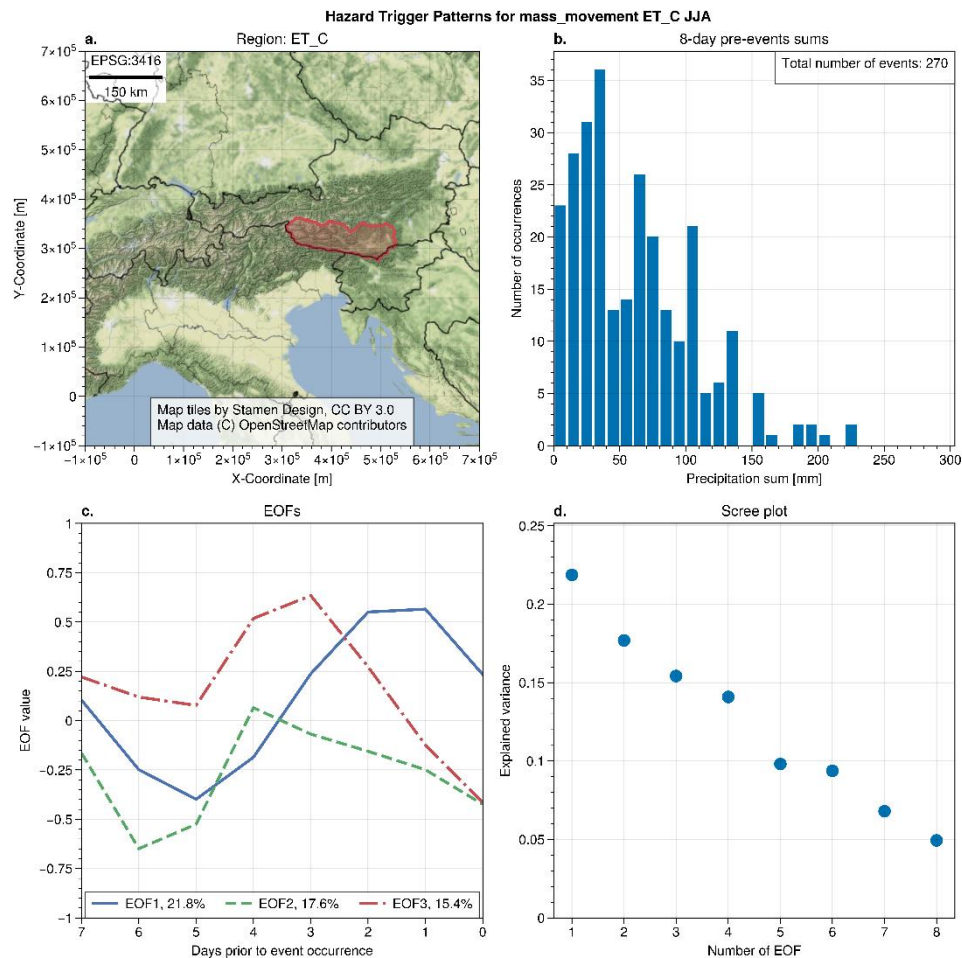


Fig. 2: Hazard Trigger Patterns for the hazard category „Mass Movement“ in the target region „East Tyrol - Carinthia“. See Fig. 1 for a description of the figure layout and content.

Results of D2.1 indicate that derived hazard trigger patterns tied to each single hazard-category-region-season combination are unique and significant, even though there are still some similarities across those combinations. Possible combinations of category, hazard and seasons total up to 16 distinct hazard trigger patterns. These are now used to investigate their potential changes in occurrence in terms of frequency until the end of the century with respect to different pathways of mankind.

## 2. DATA

### GCM DATA

GCM data were taken from the CMIP6 (Coupled Model Intercomparison Project 6) and follow the categorization into SSPs (Shared Socioeconomic Pathways). The four main scenarios of CMIP6 are SSP1-RCP2.6, SSP2-RCP4.5, SSP3-RCP3.70, SSP5-RCP8.5. In this study, the two scenarios SSP1-RCP2.6 and SSP3-RCP3.70 are considered, representing a climate-friendly and a carbon fossil fuels intensive scenario respectively. The first digit represents the socio-economic scenario (SSP1 for sustainability, SSP2 for the "middle of the road" path, SSP3 for regional rivalries, SSP5 for fossil

development) and the last two numbers indicate the radiative forcing in  $\text{W/m}^2$ . A comparison between SSP scenarios and the RCP (Representative Concentration Pathways) scenarios known from CMIP5 is shown in Figure 3 (Riahi et al., 2016). The use of the aforementioned SSP scenarios (SSP1-2.6, SSP3-3.70) covers a plausible range of potential developments.

To be able to downscale the data, various large-scale fields are needed. In the employed analog method we make use of the following variables: geopotential height at 500 hPa (zg500), air temperature at 500 hPa (ta500) and specific humidity at 500 hPa (hus500). Additionally, sea level air pressure is needed to perform GCM evaluation analysis.

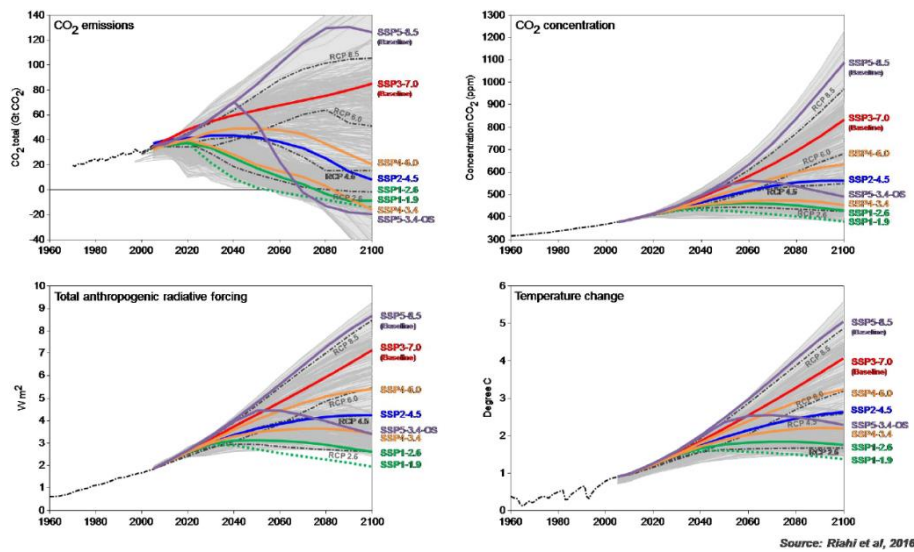


Fig. 3: Comparison between RCP and SSP scenarios for different parameters (Riahi et al., 2016)

## OBSERVATIONAL DATA - SPARTACUS

Weather data are taken from SPARTACUS, the “Spatiotemporal Reanalysis Dataset for Climate in Austria” (Hiebl and Frei 2017). It provides high quality, daily temperatures and precipitation-totals from 1961 onwards on a 1 km grid across Austria and South Tyrol. SPARTACUS has been generated in an international collaboration from irregularly distributed weather stations maintained by ZAMG, has already found application in several studies (Duethmann and Blöschl, 2018; Schroeer and Kirchengast, 2018) and is operationally kept up-to-date at ZAMG (Enigl et al., 2019).

## REANALYSIS DATA – JRA55

The JRA-55 reanalysis dataset (Kobayashi et al., 2015) spans the time period from 1958 onwards up to the present. It represents a long time period that uses the full observation system from local station data up to remote satellite information. Compared to other products, JRA-55 is the first reanalysis that employs 4DVar for data assimilation. It also incorporates a new variational bias correction for satellite data. Other improvements encompass a reduced bias of the stratospheric temperature as well as the consistency of the temperature analysis.

The same variables that are needed from the GCM data are also needed for the reanalysis data for the downscaling process and the GCM evaluation: geopotential height at 500 hPa (zg500), air temperature at 500 hPa (ta500), specific humidity at 500 hPa (hus500) and sea level air pressure.

### 3. METHODOLOGY

#### QUALITY CONTROL OF GCMs

Global datasets from GCMs may feature regional differences. Since a correct simulation of the relevant influences for Central Europe is essential for downscaling global data to a regional scale, GCMs are examined according to their corresponding skill. Two specifications are employed for this endeavour:

- PC-based NAO index (Hurrell and Deser, 2009);
- Central-European-Zonal-Index (CEZI, Jacobbeit et al., 2003).

Since the usual NAO (North Atlantic Oscillation) index is calculated from the air pressure difference between two stations, the PC-based NAO (Principal Component-based) index is particularly useful due to its applicability to model data. The calculation via a Principal Component Analysis (PCA), however, does not only allow the comparison of the indices but also the comparison of the spatial patterns (first EOF) between model and observed data (GCM and reanalysis). For the determination of the PC-based NAO index, we use anomalies of air pressure at sea level on a daily basis between 20°-80°N and 90°W-40°E (Hurrell and Deser, 2009). Subdivided by seasons, they serve as input for the EOF analysis. The same procedure is applied to the JRA-55 reanalysis dataset, which is subsequently utilized for a comparison to the GCM data. The first EOF (spatial pattern), as well as the Principal Components (PCs, time series of the expression of the spatial pattern, which represents the NAO index) are further considered for the calculation of various metrics. By employing the PCs, we determine the ratio of the standard deviation of GCM and reanalysis, the ratio of the quartile coefficient of dispersion of GCM and reanalysis, and the ratio of the explained variance of GCM and reanalysis (GCM value in the numerator, reanalysis in the denominator). The first EOF represents the spatial dipole of the maximum variance. Here, three aspects are examined:

- a) the position of the dipole center of gravity;
- b) the strength of the gradient of the dipole;
- c) the angle of the dipole axis.

Considering the first aspect, the center of gravity must be determined. For this purpose, we interpolate the values of the first EOF to a line between the two dipole centers. The mean value of all values of this line represents the center of gravity. Subsequently, we calculate the difference of the location vectors of the respective centers of gravity between GCM and reanalysis. Based on this



difference vector, the Euclidean norm is determined. The resulting value represents the corresponding metric for a). For b) the difference between the two values of the dipole center is calculated (maximum value minus minimum value). This difference is further divided by the Euclidean norm of the difference vector of the two centers, thereby corresponding to the inverse gradient vector. The direction, however, is not of particular importance, since our focus lies on its norm, i.e., the strength of the gradient. This procedure is conducted for both GCM and reanalysis data. As a last step, the resulting value from the GCM data is divided by that of the reanalysis. The result of this calculation corresponds to the metric for b). Lastly, for c), the inverse gradient vector calculated from b) can be used. Here, we form the angle between this vector and East. The metric relevant for c) is the difference between the GCM's angle and that of the reanalysis.

The Central-European-Zonal-Index (CEZI) is also determined from sea level air pressure anomalies. For its computation, we first calculate normalized seasonal anomalies. Subsequently, four spatial points are considered for a mean value calculation for two latitudinal bands (A: [35°N/0°E], [35°N/20°E], [40°N/0°E], [40°N/20°E], and B: [60°N/0°E], [60°N/20°E], [65°N/0°E], [65°N/20°E] - grid points + 2.5° delta in latitudinal and longitudinal direction; see Jacobeit et al, 2003 for further details). As a last step, we subtract the resulting mean values A, B from each other, yielding the CEZI. This procedure is conducted for both GCM and reanalysis. The metric to be examined is the standard deviation of GCM divided by the standard deviation of reanalysis, seasonally grouped, and the same for the quartile coefficient of dispersion.

Of all the metrics listed (two from the PCs, once the explained variance, three from the first EOF, and two from the CEZI), two and four times the standard deviation are calculated for all GCM models under investigation - i.e. over the full GCM ensemble. This is done for all seasons and for the model-based mean across seasons. In the case of the EOF metric (a) (one-sided value mapping), we compare the metrics for each model and season to four times the standard deviation. For all other metrics, we compare to two times the standard deviation (two-sided value mapping). If any of the values in any of the seasons is outside those thresholds, then that model is assigned an "insufficient skill" predicate.

## DOWNSCALING

In order to downscale large-scale GCMs, the analog method is applied. It is a model that represents a so-called "perfect prognosis" approach. For its calibration, we couple predictors on the large-scale to those on the local-scale by using the observation dataset SPARTACUS (Hiebl and Frei, 2016). The calibrated model is subsequently applied to the large-scale predictors of the GCMs (zg500, ta500, hus500). The application of the analogue method happens on a daily basis, with a moving window around the current investigated day, running through the whole year. For each of those subsets, a principal component analysis is conducted. We compute the Euclidean norm of the principal components between GCMs and the JRA-55 reanalysis dataset as a measure to identify suitable analogs. For the integration of a stochastic element, the analogue of a given day is randomly chosen out of the 10 best analogues. A general description of the analog method can be found in Zorita and von Storch (1999); the built-in random component is described in Beersma and Buishand (2003). The parameters of the analogue method approach can be described as follows:

- Grid weighting for EOF analysis: cosine latitude weights;



- Explained variance of EOF analysis: > 90%;
- Window width: 30 days;
- Predictors:
  - For precipitation totals: specific humidity 500 hPa, temperature 500 hPa, geopotential height 500 hPa

By means of the GCM CanESM5-historical-r1i1p1f1, we illustrate the explained variance and the number of EOFs required to downscale temperature and precipitation per day of year in Figure 4, left panel and right panel respectively.

The maximum number of EOFs needed to be taken into account is much higher in summer, which can be explained by the more structured spatial expressions in the form of convective activity. Thus, more EOFs are necessary to capture the variance in the underlying fields and to reach the explained variance threshold of 90%. This behaviour can be seen for both cases, temperature as well as precipitation, but due to the nature of precipitation fields being much more pronounced than the comparably smooth temperature fields, the number of EOFs needed for precipitation is generally higher. Especially the seasonal pattern is more distinct for the case of precipitation, which is more affected by convective activity. While the difference in the number of EOFs for temperature is only 20% (from 10 to 12) from minimum to maximum, it is over 100% for precipitation (from 18 to 38). This reflects the more difficult mapping of the model for the precipitation field, which inherently features more complex patterns than the temperature field due to its non-smooth nature and non-stationarity.

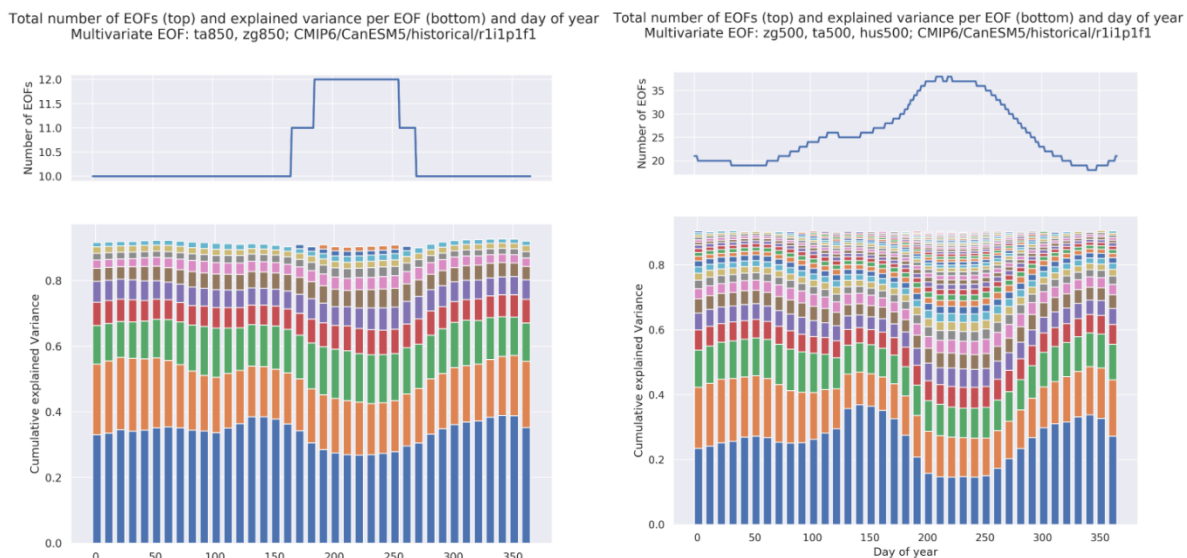


Fig. 4: Number of EOFs (top) and associated explained variance (bottom) for multivariate EOF of temperature predictors (left) and precipitation predictors (right).

For the historical time period of 1981-2010, we make use of the following verification measures:  
Regarding both temperature and minimum temperature, the absolute bias

$$absolute\ bias = |x_{model} - x_{obs}|$$

and in case of precipitation the relative bias

$$relative\ bias = \frac{|x_{model} - x_{obs}|}{x_{obs}}$$

of annual means are employed;  $|\cdot|$  indicates the mean over time.

## DERIVATION OF HAZARD DEVELOPMENT CORRIDORS AND CLIMATE CHANGE ASSESSMENT

In general, there are two focal points for future hazard development: Frequency and intensity. Both aspects share equal importance for risk reduction, as e.g., in the case of flooding. Successive hazard-events of medium intensity (i.e. higher frequency) can be just as devastating as one hazard-event with higher intensity. Furthermore, there are more faceted aspects to be considered, as higher intensity can simply be exhibited as higher values per fixed spatial extent, larger affected areas, or both.

The use of Hazard Trigger Patterns (HTPs; for details refer to D2.1) for the evaluation of potential hazard development is a two-step process:

The first step consists of defining the current climate state. Therefore, so-called “potential events” need to be determined in the past period. Potential events are events, that potentially could have caused damages due to the precedent weather evolution, but eventually did not.

HTPs originate from an PCA analysis of a two-dimensional matrix containing precipitation evolutions prior event occurrences (n rows for n events and precipitation values over 8 days in the precedent week) and represent the eigenvectors of this matrix. The corresponding “time coefficients” are referred to as “principal components (PCs)”. Methodologically, potential events can be identified by projecting meteorological data into the EOF space, generating so-called Pseudo Principal Components (PPCs). Subsequently, we compare the PPCs to the PCs from the observational data. A potential event is registered if the corresponding PPCs are within a certain Euclidean distance to the PCs. We determine the value of this distance by conducting a leave-one-out cross-validation procedure to evaluate the average distance between the PCs of the observations. This is done by iterating over all observations and computing the EOF analysis for all but one observation in each iteration. PPCs are then calculated for the omitted observation and the Euclidean distance to all PCs is computed. In each iteration step, we store the minimum of these distances. Finally, all iterations are averaged and the resulting value represents the threshold below which PPCs are counted as a potential event. The second step comprises the application of the same procedure as in step one to climate projections and the computation of hazard development corridors (HDCs). For a timeseries of the corresponding predictors of a grid point (or analogous to the HTP calculation: mean value over the respective grid point and the four adjacent grid points), a matrix is created that contains each possible 8-day sequence of this timeseries. This guarantees that all possible potential events can actually be found. This matrix is then transformed into the EOF space, generating PPCs for each of these 8-day sequences. By using the threshold value identified in step one, we can then determine for each of these sequences whether these represent a potential event. 20 random grid points per region are used to calculate the projections, which are shown in Figure 5.

The HDCs map the change in hazard potential by calculating potential events for both historical and future periods. The potential events for future periods are then normalized using the mean and standard deviation of the potential events derived in the historical period, thereby creating the so-called, hazard risk index. This index indicates the change in the hazard potential and thus represents

a quantity that can be used for risk assessment. The content of this index, however, refers purely to the frequency of the underlying phenomenon and does not describe its amplitude which may be qualitatively estimated by means of the climate indicators for the corresponding damage categories.

Some climate indicators are also calculated as area-averages over the region of interest, in order to assess the potential development of intensity for hazardous damage event. Thereby, RR20mm, Rx5day and Rx1day are used. RR20mm depicts the number of days per year in which daily precipitation totals surpassed 20 mm. Rx5day is the annualized maximal precipitation sum for 5 consecutive days and Rx1day is similarly the annualized maximal precipitation sum for 1 day. Those indicators are calculated for the historical period as well as the future period.

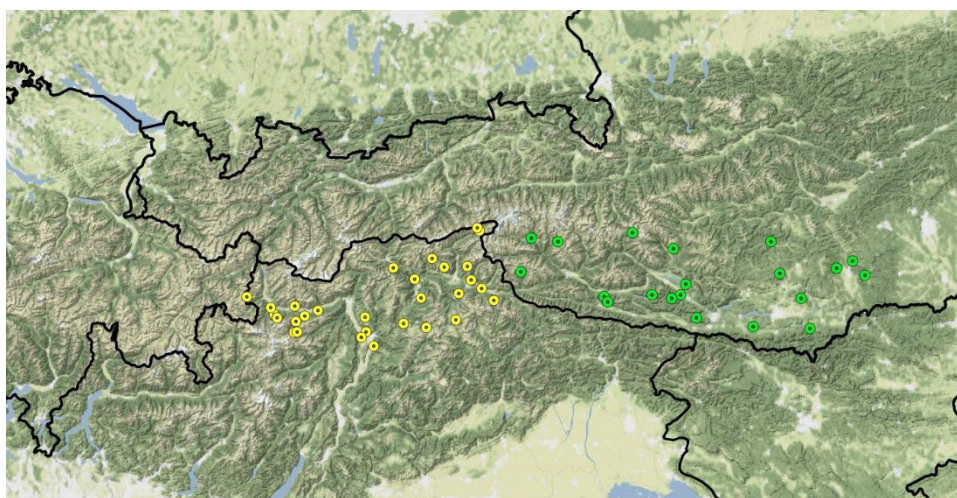


Fig. 5: The 20 randomized grid points per region that were selected for the calculation of projections for hazard development corridors. Yellow coloured markers reside in the region ST, green coloured in ET\_C.

## 4. RESULTS

### QUALITY CONTROL OF GCMs

Out of the 136 GCMs we tested, 56 remained. Some models of these, however, do not have the necessary number of variables required for further processing. This circumstance lowers the number of corresponding models to 32. The proportion of filtered models grouped by the underlying driving GCM is depicted in Figure 6 and the final list of GCMs is shown in Table 1.

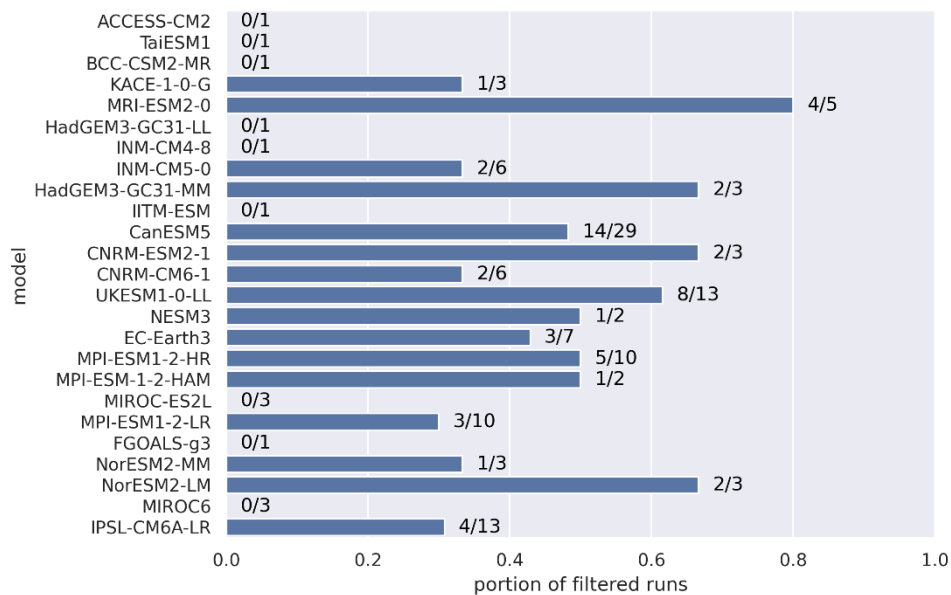


Fig. 6: Proportion of models remaining after the applied GCM evaluation, grouped by the underlying driving GCM.

Table 1: Quality controlled GCMs, n=32.

Model	Member	Model	Member	Model	Member
CanESM5	r1i1p1f1	HadGEM3-GC31-MM	r3i1p1f3	MPI-ESM1-2-HR	r2i1p1f1
CanESM5	r2i1p1f1	INM-CM5-0	r3i1p1f1	MPI-ESM1-2-HR	r3i1p1f1
CanESM5	r2 i1p2f1	INM-CM5-0	r4i1p1f1	MPI-ESM1-2-HR	r6i1p1f1
CanESM5	r5i1p2f1	IPSL-CM6A-LR	r3i1p1f1	MPI-ESM1-2-HR	r10i1p1f1
CanESM5	r9i1p1f1	IPSL-CM6A-LR	r4i1p1f1	MRI-ESM2-0	r1i1p1f1
CanESM5	r9i1p2f1	IPSL-CM6A-LR	r11i1p1f1	MRI-ESM2-0	r3i1p1f1
CanESM5	r10i1p1f1	IPSL-CM6A-LR	r14i1p1f1	MRI-ESM2-0	r4i1p1f1
CanESM5	r10i1p2f1	KACE-1-0-G	r1i1p1f1	MRI-ESM2-0	r5i1p1f1
CNRM-CM6-1	r1i1p1f2	KACE-1-0-G	r3i1p1f1	NorESM2-LM	r1i1p1f1
CNRM-CM6-1	r6i1p1f2	MPI-ESM1-2-HAM	r1i1p1f1	NorESM2-LM	r2i1p1f1
HadGEM3-GC31-MM	r1i1p1f3	MPI-ESM1-2-HR	r1i1p1f1		

## DOWNSCALING

For comparison between the models, the biases for minimum temperature and precipitation are depicted in Figures 7 and 8, respectively. Considering the results for minimum temperature, the majority of models follow a similar pattern and feature a weak warm bias. The two INM-CM5-0 models, the HadGEM3-GC31-MM/r1i1p1f3 and the MPI-ESM1-2-HR/r1i1p1f1 stand out with possessing no bias pointing in either direction. The broad scatter indicate the presence of individual outliers in each model. What is striking here is the clearly stronger expression of the warm bias. Figure 8 illustrates the precipitation bias amongst the models considered. It is characterized by a relatively homogeneous behavior across all models with a small bias towards lower annual precipitation amounts than the observation. An exception constitutes KACE-1-0-G/r3i1p1f1 as it stands out with no dominant direction of bias. The overall spread, however, is more pronounced for this model.

While the lower whisker is similar to other models, it represents the only model exhibiting an over-estimation of precipitation of well over 20%. It is essential to include the biases in regional evaluations for making adequate estimations. For further details see the clim\_ect report <sup>1</sup>.

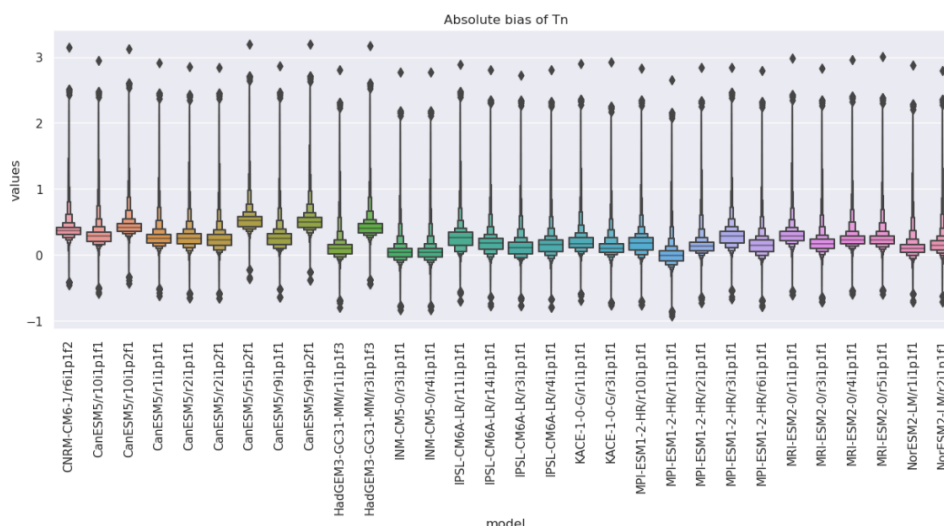


Fig. 7: Absolute bias of minimum temperature on an annual basis. Time period 1981-2010. Box plots over the whole of Austria.

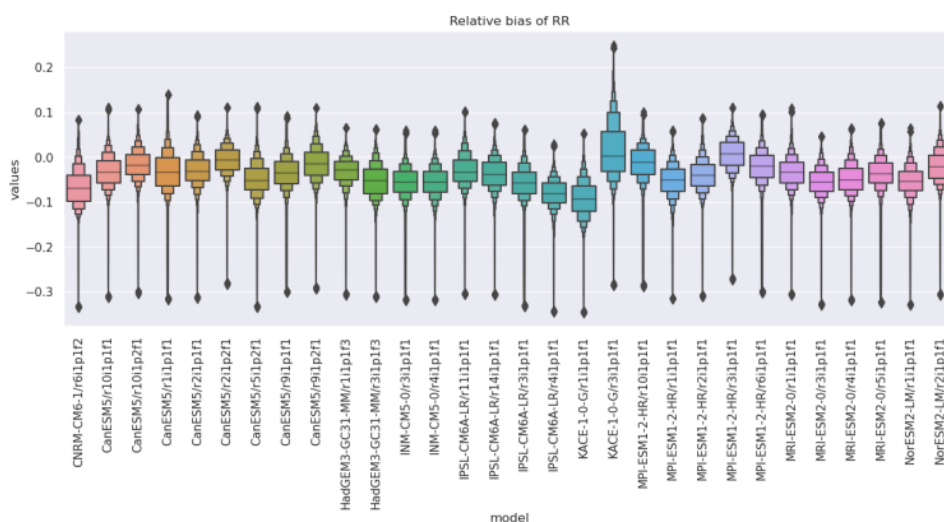


Fig. 8: Relative bias of precipitation on an annual basis. Time period 1981-2010. Box plots over the whole of Austria

From the 32 quality-controlled GCMs (Table 1), a total of 114 runs are available across the five main experiments (historical, SSP126, SSP245, SSP370, SSP585). These represent the entire quality-checked ensemble. Divided among the experiments, the distribution features 19 runs for SSP1-RCP2.6 and SSP5-RCP8.5, 20 runs for SSP2-RCP4.5, and 25 for SSP3-RCP7.0. As already outlined, for further analysis the two scenarios SSP1-RCP2.6 and SSP3-RCP7.0 are used, which cover the plausible range of possible future development.



Figure 9 shows anomalies of the annual minimum temperature related to the time period 1981 to 2010, depicting the ensemble mean as a line and the 95% confidence interval as shading. It illustrates a common picture that – in dependence of the considered scenario - different degrees of warming have to be expected. According to the physical understanding, this also influences processes that can lead to damage-triggering extreme weather events. For precipitation, normalized anomalies (anomalies divided by the standard deviation of the observation) are depicted in Figure 10. In this case, no clear picture prevails. The spread of scenarios is large, resulting in poor discriminatory power among scenarios. However, a clear tendency is evident: for precipitation, a small increase in precipitation is projected under all scenarios. This is - regardless of the fact that locally different characteristics may exist - consistent with the increase in temperature, which allows the atmosphere to hold more water vapor, an increase in precipitation is generally expected.

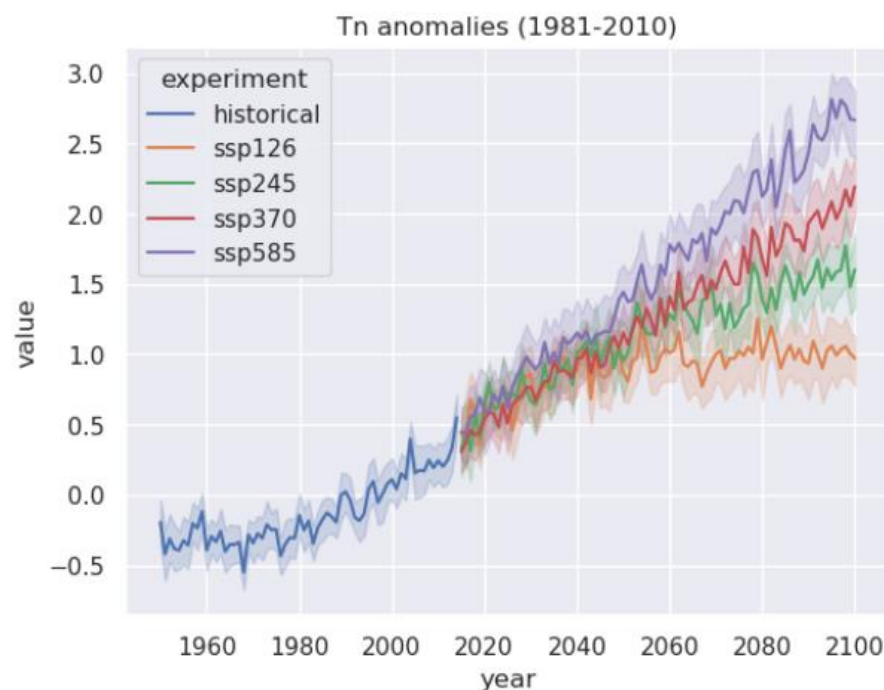


Fig. 9: Anomalies of the annual minimum temperature related to the time period 1981 to 2010.

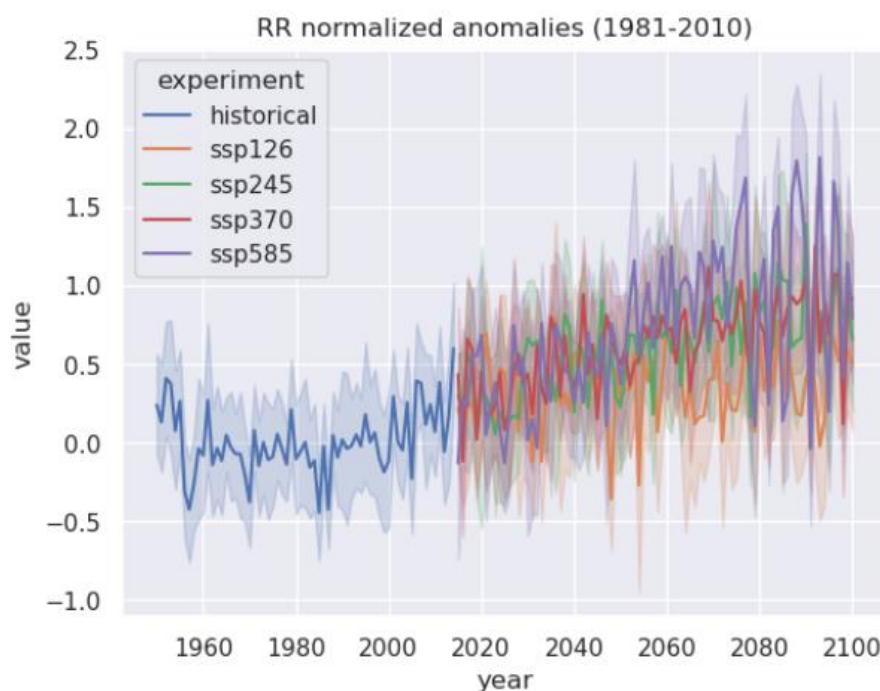


Fig. 10: Anomalies of the annual precipitation related to the time period 1981 to 2010.

## DERIVATION OF HAZARD DEVELOPMENT CORRIDORS AND CLIMATE CHANGE ASSESSMENT

The hazard development corridors (HDCs) for both categories (“flood” and “mass\_movement”) for all seasons and the region ET\_C can be seen in Figures 11 and 12. The first row depicts the four seasons DJF, JJA, MAM, and SON for “flood” and the second row the four seasons for “mass\_movement”. For the boxplots, the hazard risk index was averaged per model over the time period near\_future (2036-2065) and far\_future (2071-2100) as well as over the corresponding grid points in the region. The box and whiskers then represent the multi-model statistics per time\_period and experiment (SSP1-RCP26 in blue, SSP3-RCP70 in red). For Figure 11, the multi-model mean and for Figure 12, the multi-model 90<sup>th</sup> percentile is shown. Additionally, the dashed black horizontal line serves as reference point for a standard normal distribution. Figure 11 reveals the unique characteristics of the hazard trigger patterns, because they are based on the same meteorological predictor, but differ in results. For the season DJF and “flood” (top left subplot) there is no substantial trend. The tendency goes toward increased risk potential, but only marginally compared to the variability in the multi-model ensemble. For “mass\_movement” (bottom left subplot) the signal changes drastically. A pronounced decrease in risk potential is suggested. The corresponding hazard trigger pattern (Figure 13) shows an intensifying precipitation sequence toward the event date, with overall maximum values on the event day itself. The decrease in the hazard risk index might suggest such sequences to become scarcer. In the second column for the summer season the situation for “flood” might depict a tendency toward a decrease in risk potential, but the variability is still too large to draw final conclusions. For “mass\_movement” on the other hand again a more pronounced signal, especially in the far future can be seen. It is evident by the large variability between the



experiments though, that there is substantial natural variability superimposed on the signals, noisifying potential significant trends. The corresponding hazard trigger pattern is shown in Figure 2 and contrary to the case beforehand contains more pre-moistening components. The only other combination of parameters that suggest a tendency compared to the variability is again “mass\_movement” for the season MAM. Comparably to the situation in the season DJF, a decrease in the hazard risk index can be seen. The corresponding hazard trigger pattern is not as indicative as the two beforehand, containing elements of both pre-moistening and short-term precipitation and thereby not allowing clear-cut conclusions from what a potential decrease might originate (not shown).

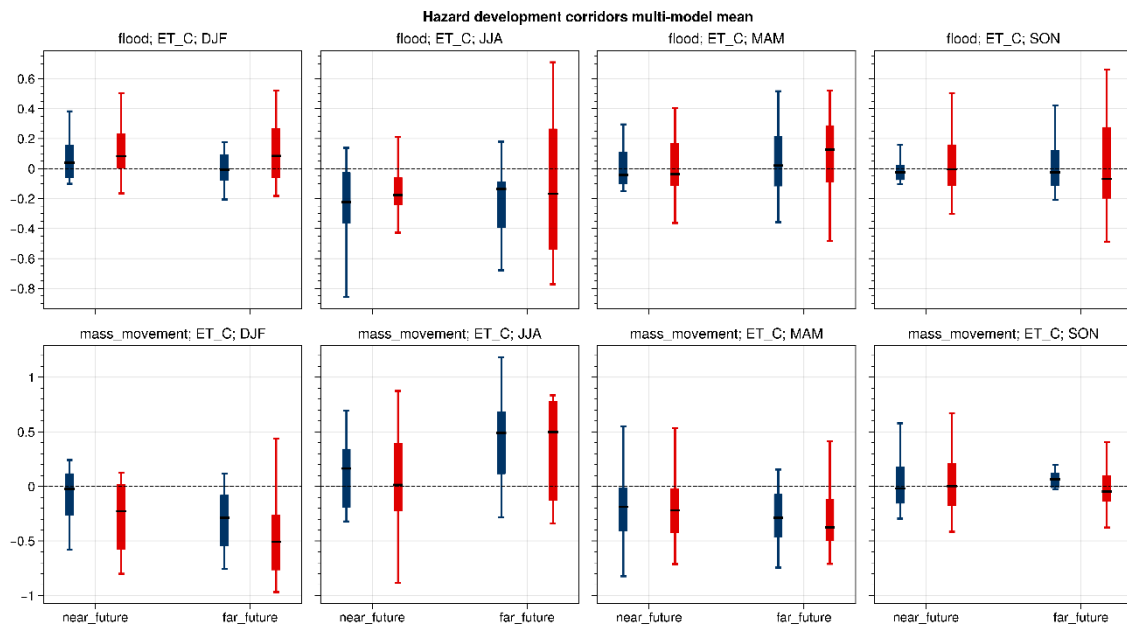


Fig. 11: HDCs for the combination of flood (top row) and mass\_movement (bottom row) for the region ET\_C and the four seasons (columns). Depicted are boxplots for GCM means of the normalized risk index for SSP1-RCP2.6 (blue) and SSP3-RCP7.0 (red) experiments, for the near (2035-2065) and far future (2071-2100). The dashed black line represents the mean for a standard normal distribution and serves as reference point.

It can not only be beneficial, but maybe even more important to not only look at the model-means, but at high percentiles. Those situations depict the most extreme cases, that potentially cause the most losses. In Figure 12 the 90<sup>th</sup> percentile of the hazard risk index for models is shown as multi-model boxplot. The dashed black horizontal line serves again as reference to a standard normal distribution, wherein the 90<sup>th</sup> percentile is at roughly 1.28. A higher/lower multi-model median hence suggests an intensifying/relaxation of high impact risk potential respectively. Looking at “flood” in the first row of Figure 12 there does not seem to be overwhelming support for a significant increase in the hazard risk index. Although, it has to be noted that the large variabilities, especially for the far\_future compared to the near\_future have to be carefully considered. This depicts some chance of a worsening development in terms of hazard event frequencies, with a larger number of potential events. For “mass\_movement” in the bottom row the signal is relatively comparable to the deductions from the multi-model means of Figure 11. Looking at the numbers for the summer season and far\_future (bottom row, second subplot from the left-hand-side) the multi-model median for the 90<sup>th</sup> percentile corresponds to roughly a value of the 97<sup>th</sup> percentile for a standard normal distribution. This is a substantial increase depicting a threefold increase in potential events

at that rarity level. The other changes are not as pronounced and especially do not show such a substantial increase for the hazard risk index. Hence this situation should be investigated more carefully, taking into account more information from other sources.

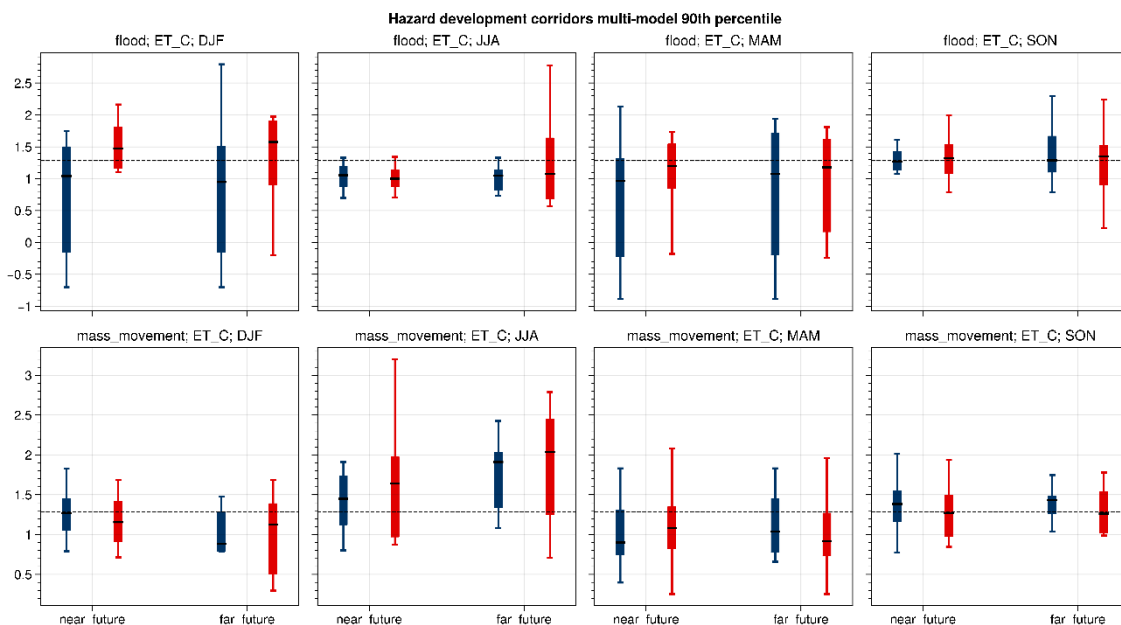


Fig. 12: Same as Figure 9, but instead of model means, the 90th percentile of the normalized risk index is shown. The dashed black line represents the 90th percentile for a standard normal distribution and serves as reference point.

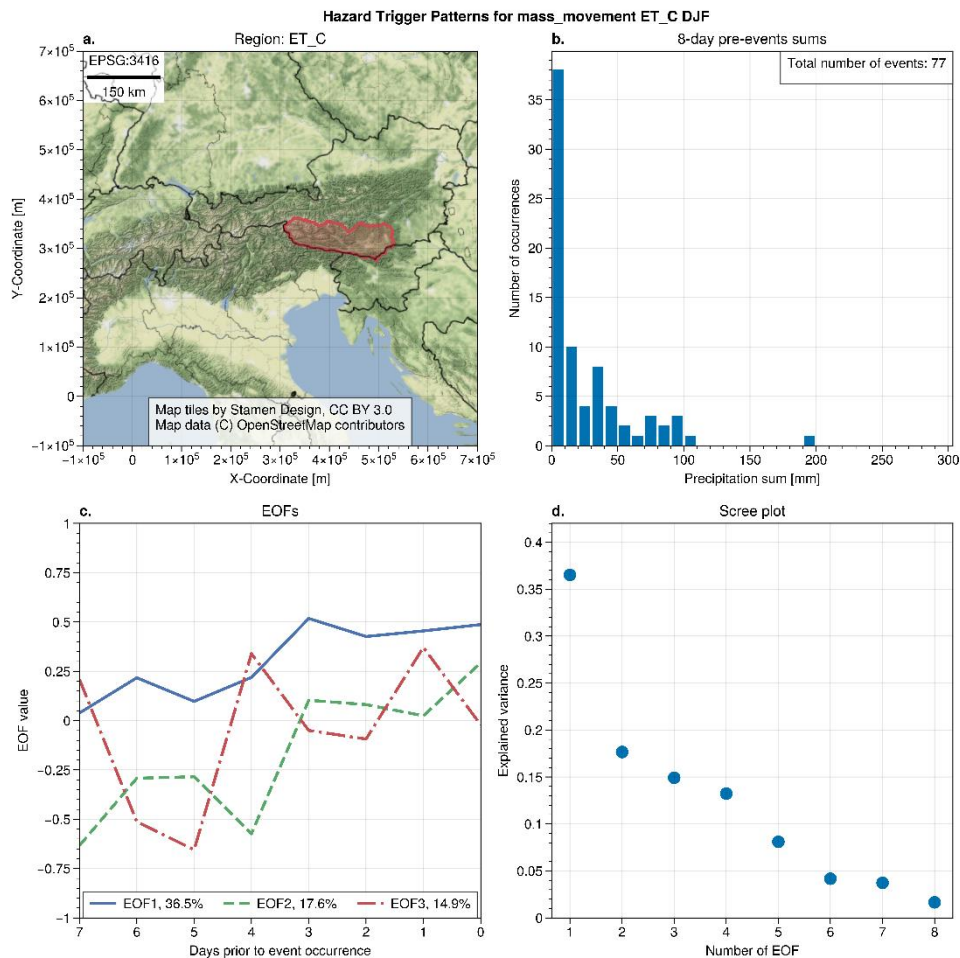


Fig. 13: Hazard trigger pattern for “mass\_movement” in the region ET\_C and season DJF.

Figures 14 to 16 depict the aforementioned climate indicators R20mm, Rx5day and Rx1day respectively, area-averaged for the Region ET\_C. It is evident, that there is no significant trend visible in either direction for neither GCM scenario. On the other hand, it can also be seen, that the variability is substantial and hence a large amount of noise superimposes and interferes with any potential signal. A small detail in Figure 12 for Rx5day though, is that the upper tail of the distribution toward the end of the century is broader than the lower tail. This might suggest an increasing intensity in consecutive 5-day-precipitation amounts. Although, it has to be noted, that the same is not as evident in the other two climate indicators, R20mm and Rx1day, to the same extent. Roughly speaking, the climate indicators might therefor suggest slightly increased chances of more extreme precipitation.

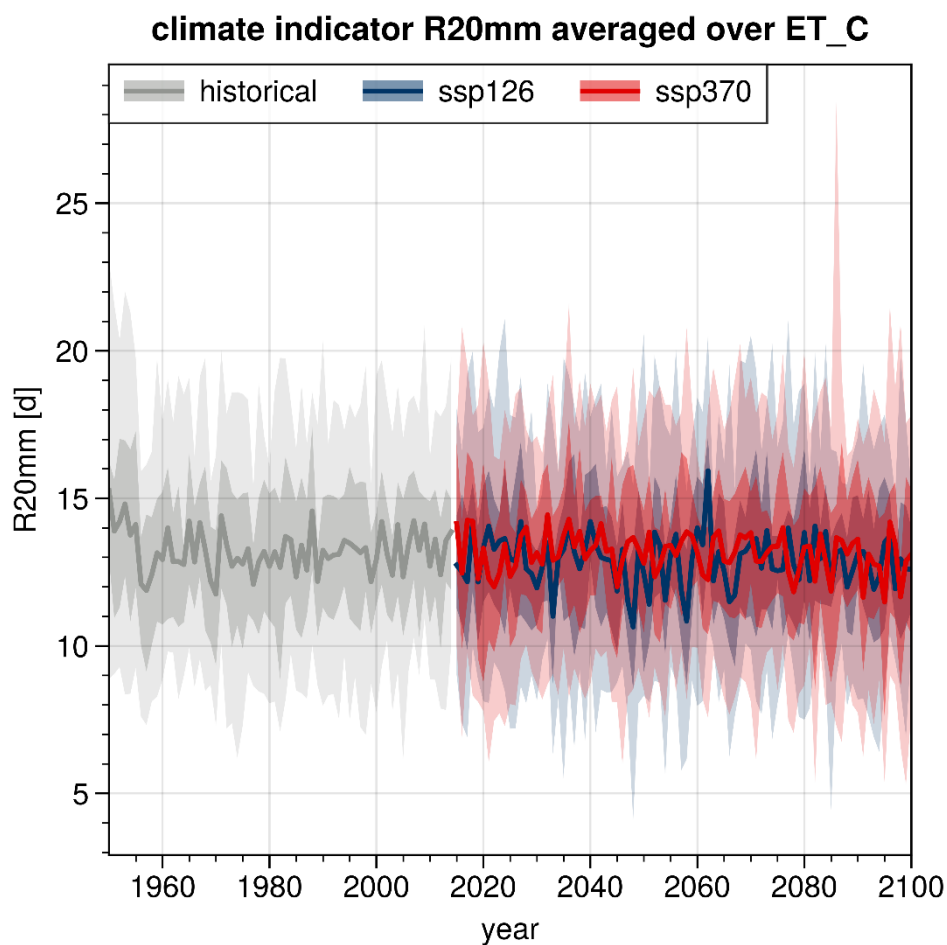


Fig. 11: Climate indicator R20mm area-averaged over ET\_C for the GCM ensemble of historical, SSP1-RCP2.6 and SSP3-RCP7.0 experiments.

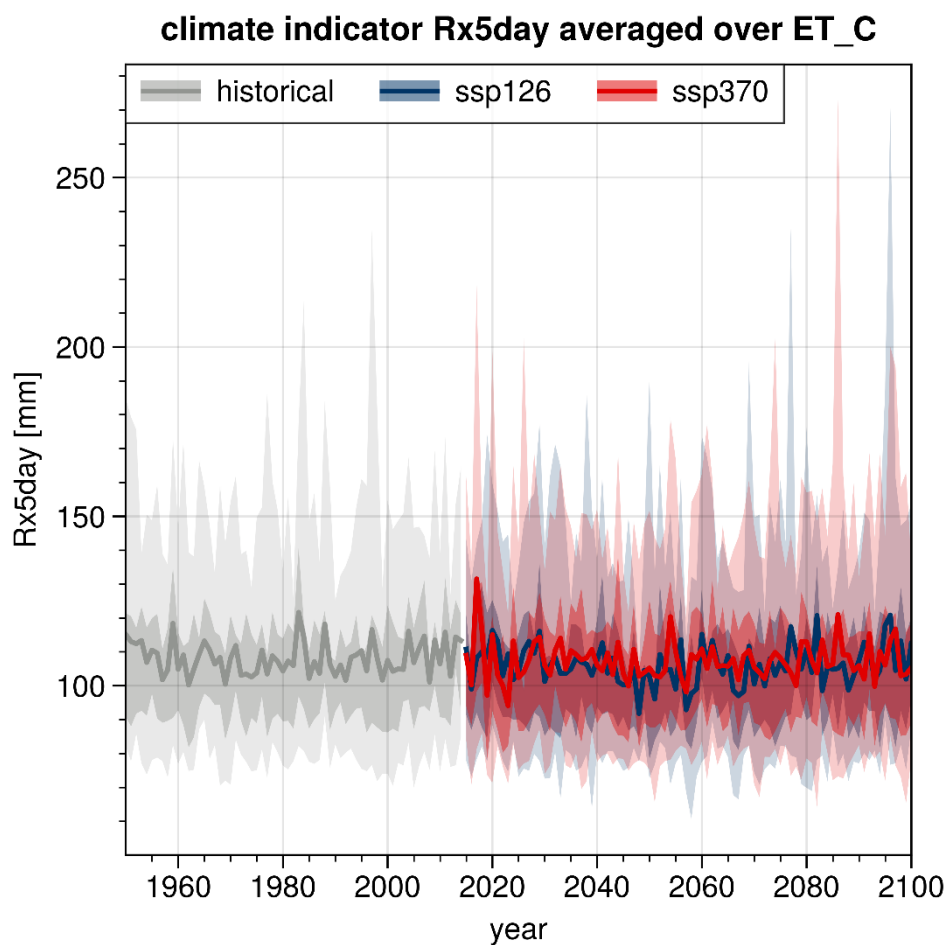


Fig. 12: Climate indicator Rx5day area-averaged over ET\_C for the GCM ensemble of historical, SSP1-RCP2.6 and SSP3-RCP7.0 experiments.

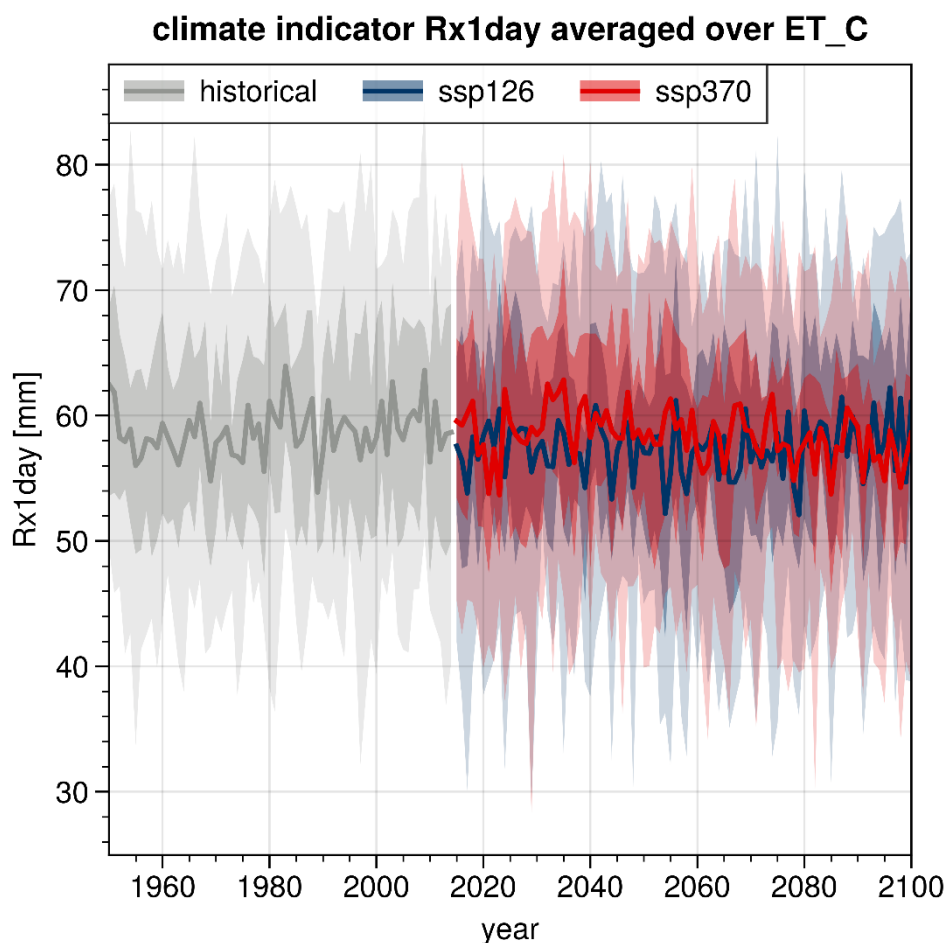


Fig. 13: Climate indicator Rx1day area-averaged over ET\_C for the GCM ensemble of historical, SSP1-RCP2.6 and SSP3-RCP7.0 experiments.

In conclusion, the results of the hazard development corridors show mixed signals with a substantial amount of superimposed noise. This is largely due to natural variability and some uncertainty originating from the methodology, due to the localized-nature of the technique. Furthermore, additional uncertainty is still present in the analysis, because of the fact that 20 randomized grid points per region were evaluated. This is a computational limitation though, as the calculation of the projections is computationally expensive. Nevertheless, previous tests have shown this to be a large enough number for finding tendencies and drawing conclusions.

All results combined, hazard development corridors, the annual potential increase in precipitation and the large fluctuations in high-impact climate indicators, it is evident that potential future risk increases have to be taken into consideration for high-impact assessments. The most damage is not done by the averages of the distributions, but by extremes and superimposed extreme states that are further escalated by a tendency of increasing risk potential in certain situations outlined above, which may have devastating consequences if not taken into consideration.

## 5. REFERENCES

Beersma, Jules J., and T. Adri Buishand, 2003. "Multi-site simulation of daily precipitation and temperature conditional on the atmospheric circulation." *Climate Research*. 121- 133.

Duethmann, D., Blöschl, G., 2018. Why has catchment evaporation increased in the past 40 years? a data-based study in Austria. *HHydrol. Earth Syst. Sci.* 22 (10), 5143–5158. <https://doi.org/10.5194/hess-22-5143-2018>.

Hiebl, J., Frei, C., 2017. Daily precipitation grids for Austria since 1961 – development and evaluation of a spatial dataset for hydroclimatic monitoring and modelling. *Theor. Appl. Climatol.* 132, 327–345. <https://doi.org/10.1007/s00704-017-2093-x>.

Hurrell, J. W., Deser C., 2010 "North Atlantic climate variability: the role of the North Atlantic Oscillation." *Journal of Marine Systems*. 79.3-4: 231-244.

Jacobeit, J., et al. (2003) "Atmospheric circulation variability in the North-Atlantic-European area since the mid-seventeenth century." *Climate Dynamics* 20.4: 341-352.

Kobayashi, Shinya & Ota, Yukinari & Harada, Yayoi & Ebita, Ayataka & Moriya, Masami & Onoda, Hirokatsu & Onogi, Kazutoshi & Kamahori, Hirotaka & Kobayashi, Chiaki & Endo, Hirokazu & Miyaoka, Kengo & Takahashi, Kiyotoshi. (2015). The JRA-55 Reanalysis: General Specifications and Basic Characteristics. *Journal of the Meteorological Society of Japan*. 93. 5-48. 10.2151/jmsj.2015-001.

Schroeder, K., Kirchengast, G., 2018. Sensitivity of extreme precipitation to temperature: the variability of scaling factors from a region to local perspective. *Clim. Dyn.* 50, 3981–3994. <https://doi.org/10.1007/s00382-017-3857-9>

Von Storch, H., and F. W. Zwiers, 1999. Statistical analysis in climatology, Cambridge.

Zorita, E., Von Storch H., 1999. The analog method as a simple statistical downscaling technique: Comparison with more complicated methods. *Journal of Climate*. 2474-2489.